TJNN Thai Journal of Nanoscience and Nanotechnology

Effect of Al Dopant on Physical and Optical Properties of Er-Doped CuS Prepared by Co-Precipitation Process

Junkrajang Wattana[1,*], Pakkawat nimitnopphasit[1], Thanaphon Kansaard[1], Kanokthip Boonyarattanakalin[1], Wanichaya Mekprasart[1], C.K. Jayasankar[2], and Weerachon Phoohinkong[3]

[1]School of Integrated Innovative Technology, King Mongkut's Institute of Technology Ladkrabang, Bangkok, 10520, Thailand
[2]Department of Physics, Sri Venkateswara University, Tirupati, 517 502, India
[3]Faculty of Science and Technology, Suan Dusit University, Bangkok, 10300, Thailand

Received: 31 May 2025, Revised: 26 June 2025, Accepted: 28 June 2025

Abstract

Considering the pressing demand for energy conservation, sustainable solutions in the building sector have become paramount. This study focuses on the development of sustainable, energy-efficient technologies for window glasses and transparent solar shielding film materials. The primary objective is to achieve a delicate balance: enabling the transmission of visible light while effectively shielding against Near Infrared Radiation (NIR). Copper sulfide (CuS) emerges as a promising p-type semiconductor material due to its favorable NIR shielding performance. In this research, CuS particles were synthesized via a simple co-precipitation method. Additionally, with certain dopant ratios of erbium (Er) as rare earth dopants and the various dopant ratios of aluminum (Al), explore the enhancement of the solar spectral selectivity. The X-ray diffraction technique was used to characterize the crystalline structure of the synthesized powders, while X-ray photoelectron spectroscopy was utilized to explore the valence states of the samples. Furthermore, the optical properties of the synthesized powders and prepared thin films were observed using a diffuse reflectance spectrophotometer. Lastly, the thermal insulation performance of the prepared thin films was evaluated using a custom device, supplemented by an infrared lamp. The NIR shielding performance was assessed by examining the lowest transmittance in the NIR region, attributed to changes in the valence state induced by the dopant, thereby enhancing the semiconducting behavior of CuS.

Keywords: Near infrared shielding, Copper sulfide, Erbium, Aluminum, Co-precipitation method

1. Introduction

Nowadays, energy-saving technologies have drawn large amounts of attention due to the increase in energy consumption in every departure from previous years [1]. Buildings account for approximately 40% of total energy consumption, largely attributed to the low shielding performance of conventional windows [2]. These windows can primarily reduce brightness from the external environment but have low performance to effectively block intense solar radiation, particularly in the ultraviolet (UV) and near-infrared (NIR) regions [3]-[5], which contribute about 4% and 57% of solar energy, respectively. This results in indoor temperatures rising beyond human comfort levels, extensively increasing the usage of air conditioning, especially in tropical and subtropical regions [3]-[6]. Therefore, the development of energy-saving technologies to enhance thermal insulation efficiency has become an urgent priority. NIR shielding technologies such as transparent solar shielding materials [7]-[13] were developed, and various types of NIR shielding material such as indium tin oxide (ITO), antimony tin oxide (ATO), lanthanum hexaboride (LaB_6), tungsten bronze, and copper sulfide (CuS) [14]-[24] were used.

Among them, CuS is a p-type semiconductor that has a band gap energy in the range of 1.2-2.6 eV. It not only has good chemical and electric properties but also has a brilliant performance as a photocatalyst and is non-toxic with low-cost material [25]-[27]. Previous reports showed that its high

Corresponding Author: 67116001@kmitl.ac.th

hole carrier concentration due to p-type semiconductor properties also made the material exhibit strong localized surface plasmon resonance (LSPR), leading to the enhancement of NIR absorption performance [28]-[32]. These properties lead to its good electrochemical performance and NIR shielding properties, which can be further enhanced by various types of methods. There are many phase structures of copper sulfide, just like villamaninite (CuS_2), yarrowite ($Cu_{1.12}S$), spionkopite ($Cu_{1.39}S$), geerite ($Cu_{1.6}S$), anilite ($Cu_{1.75}S$), digenite ($Cu_{1.8}S$), djurleite ($Cu_{1.96}S$), chalcocite (Cu_2S), and covellite (CuS) [33]. Therefore, covellite CuS is the structure that shows the strongest LSPR in the NIR region due to its highest hole concentration compared to all structures [33]-[35]. Hence, enhancement of the NIR shielding performance can be done by increasing the hole concentration of the materials. Doping with metal ions is one of the candidate methods since it can adjust and control free carrier concentration and optical properties of materials by introducing new energy levels within the band gap, also it is compatible with simple and low-cost synthesis methods like the co-precipitation method which needed lower temperatures than others method like solvothermal or hydrothermal methods to receive a controllably particle size and stoichiometric structure [36]-[38].

For the enhancement of NIR shielding performance, Er and Al dopants were used. Erbium dopant is a lanthanide, a rare earth metal that possesses 4f electrons with specific energy levels that enable transitions in the NIR range between $^4I_{13/2}$ and $^4I_{15/2}$, leading to strong absorption at 1540 nm [39]-[40]. These properties make Er^{3+} complexes valuable for NIR shielding. Meanwhile, Al dopant is a high ductility, malleability, low density, corrosion-resistant, good electrical dopant that was used as a p-type dopant for semiconductors, leading to the creation of hole carriers in the material lattice while substituting the material ions [41]. In this case, Al^{3+} dopants will be capable of substituting the Cu^{2+} ions of CuS since their ionic radii are nearly the same. The dual doping was meant to improve the NIR shielding performance of CuS particles while maintaining structural stability.

In this research, we focused on Er/Al co-doped CuS particles synthesized with a constant Er dopant at 10 mol% while varying Al dopant concentrations via the co-precipitation method to demonstrate the enhancement of NIR shielding properties of the material. The crystal structures, elemental analysis, chemical composition, optical properties, and thermal insulation performance of the synthesized Er/Al co-doped CuS samples were investigated. Expecting that this material can be a candidate for improving light-shielding film in the future.

2. Experimental

2.1 Materials

Copper (II) nitrate trihydrate ($Cu(NO_3)_2{\cdot}3H_2O$), thiourea (CH_4N_2S), erbium (III) nitrate pentahydrate ($(ErNO_3)_3{\cdot}5H_2O$, and aluminum (III) nitrate nonahydrate ($(AlNO_3)_3 \cdot 9H_2O$) were used as starting materials. Diethanolamine (DEA, $C_4H_{11}NO_2$) and isopropyl alcohol (IPA, C_3H_8O) were used as capping agents. Deionized water was used as a solvent. Ammonia (NH_3) was used for pH adjustment. Polyvinyl alcohol ($(C_2H_4O)_n$, PVA) was used as a binder for film coating. All chemicals in this study were analytical grade and used in experiments.

2.2 Preparation of Er/Al-doped CuS particles

For the synthesis of Er/Al-doped CuS particles, 0.1 mol of copper (II) nitrate trihydrate ($Cu(NO_3)_2{\cdot}3H_2O$), 0.01 mol of erbium (III) nitrate pentahydrate ($(ErNO_3)_3{\cdot}5H_2O$, and a certain amount of aluminum (III) nitrate nonahydrate ($(AlNO_3)_3 \cdot 9H_2O$) were dissolved in 200mL of DI water. Then, 4 mL of DEA and 8 mL of IPA were added and stirred for 30 minutes at a constant temperature of 70 °C (pH = 8). Next, 0.1 mol of thiourea was mixed with the solutions and stirred for 2 hours at a constant temperature of 70 °C (pH = 10). Finally, the as-obtained particles were washed with DI water until pH = 7 and dried overnight at 100 °C to receive Er/Al-doped CuS particles. The Er content in the precursor was fixed at 10 mol%, and Al composition mol ratios were varied at 0, 0.02, 0.04, 0.06, and 0.08. The corresponding samples are denoted as CuS, CuSEr10%, CuSEr10%Al2%, CuSEr10%Al4%, CuSEr10%Al6%, and CuSEr10%Al8%, respectively.

2.3 Preparation of Er/Al-doped CuS films

PVA was dissolved in DI water to get a 10 wt% PVA solution. Thereafter, 0.15g of Er/Al-doped CuS particles were dispersed in the dark-green slurry. The coating slurry was then cast onto the glass. Finally, the coated glasses were dried at 70 °C until dry.

2.4 Characterization

The crystal structure of the synthesized samples was determined by the X-Ray Diffractometer (XRD, Rigaku, SmartLab) equipped with Cu-Kα radiation. The elemental analysis and composition analysis of the samples were investigated by X-ray Photoelectron Spectroscopy (XPS, ULVAC-PHI, JEOL JSM-7610F). The optical property of the particles and films was measured by a UV-VIS-NIR Spectrophotometer (UV-VIS-NIR, HITACHI, UH4150) in the range of 250-1500 nm. The thermal shielding properties of Er/Al co-doped CuS films were evaluated by a home-made device with a 100 W infrared lamp, as shown in Fig.1.

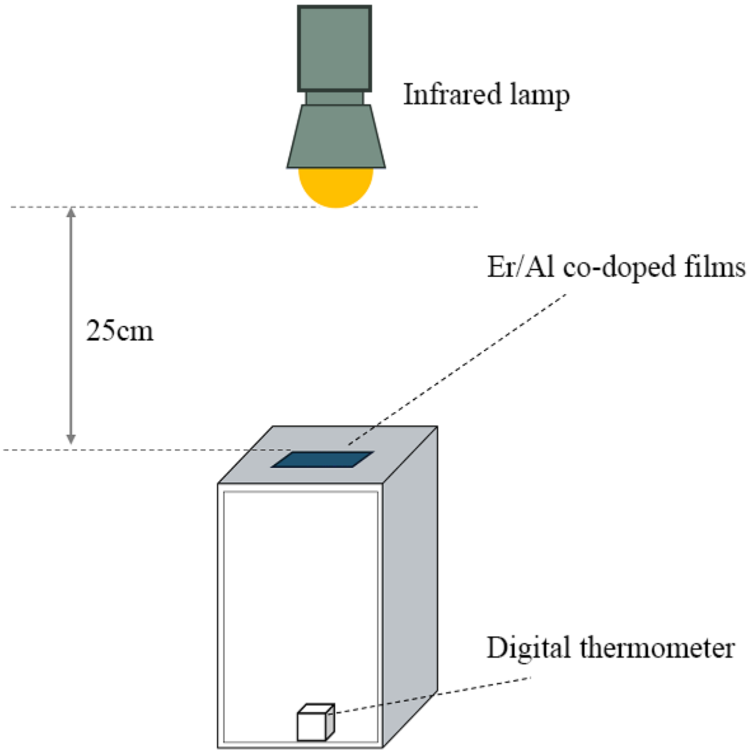

Fig. 1. Schematic diagram of the device used for the thermal insulation performance testing.

3. Result and discussion

3.1 Structure and composition analysis of Er/Al co-doped CuS particles

Fig. 2 shows the XRD patterns of CuS and Er/Al co-doped CuS with different doping amounts of Al prepared by the co-precipitation method. The peaks of CuS at 27.7°, 29.4°, 31.9°, 32.8°, 48.0°, 52.8°, and 59.4° referred to the (101), (102), (103), (006), (110), (108), and (116) planes of the hexagonal CuS structure [JCPDS No: 03-065-3561], respectively. These peaks also appeared for Er-doped CuS and Er/Al co-doped CuS particles, indicating the maintenance of the covellite hexagonal CuS structure, except for the (116) plane. The disappearance of the (116) plane may have occurred from the replacement of the dopants in the lattice [42]. The crystallite size and lattice parameter are calculated using the following formulas for more information.

$$D = \frac{0.9\lambda}{\beta \cos\theta} \tag{1}$$

$$\frac{1}{d^2} = \left(\frac{h^2+k^2}{a^2}\right) + \left(\frac{l^2}{c^2}\right) \tag{2}$$

where D is the crystalline size of particles, λ is the X-ray wavelength (Cu-Kα), β is the full width at half maximum (FWHM), θ is the Bragg angle, d is the interplanar spacing, h, k, and l are the Miller indices, and a and c are lattice constants.

As we can see, Table 1 shows that the crystalline size of CuSEr10% has the lowest value compared to other conditions. Combined with the disappearance of the (006) hexagonal CuS plane in CuSEr10%, we can assume that due to the larger ionic radius of Er^{3+} (114 pm) than Cu^{2+} (71 pm), the interstitial site of Er ions interrupted the formation of lattice crystalline, decreasing its crystalline size and increasing d-spacing in the lattice, causing the lower angle shift while remaining as a hexagonal CuS structure [38]. Lattice parameter c is increasing when there are dopants in the lattice, resulting from the interstice of Er ions, which causes lattice expansion due to the difference in ionic radii and local lattice distortion. Meanwhile, the increasing lattice strain can be attributed to the appearance of dopants in the lattice, further confirming the interrupted formation of lattice crystalline, which leads to the decrease of crystalline size.

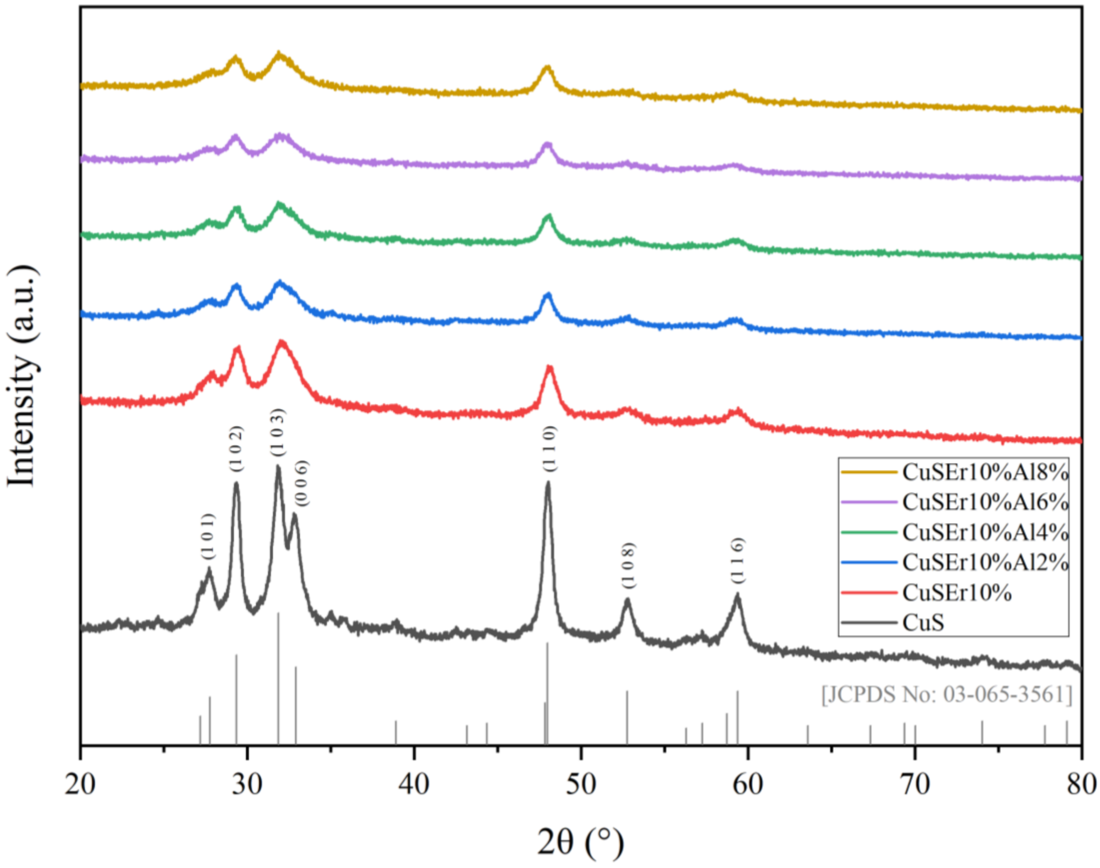

Fig. 2. XRD patterns of CuS and Er/Al co-doped CuS particles with different doping amounts of Al prepared by the co-precipitation method.

Table 1. Crystallite size and lattice parameter (a, b, c) of CuS and Er/Al co-doped CuS particles

Sample	**Crystalline size (nm)**	**a = b (Å)**	**c (Å)**	Strain
CuS	80	4.26	6.59	0.0019
CuSEr10%	29	5.60	17.65	0.0061
CuSEr10%Al2%	31	3.80	16.15	0.0058
CuSEr10%Al4%	31	3.79	16.14	0.0060
CuSEr10%Al6%	32	3.76	17.10	0.0060
CuSEr10%Al8%	35	4.13	15.48	0.0047

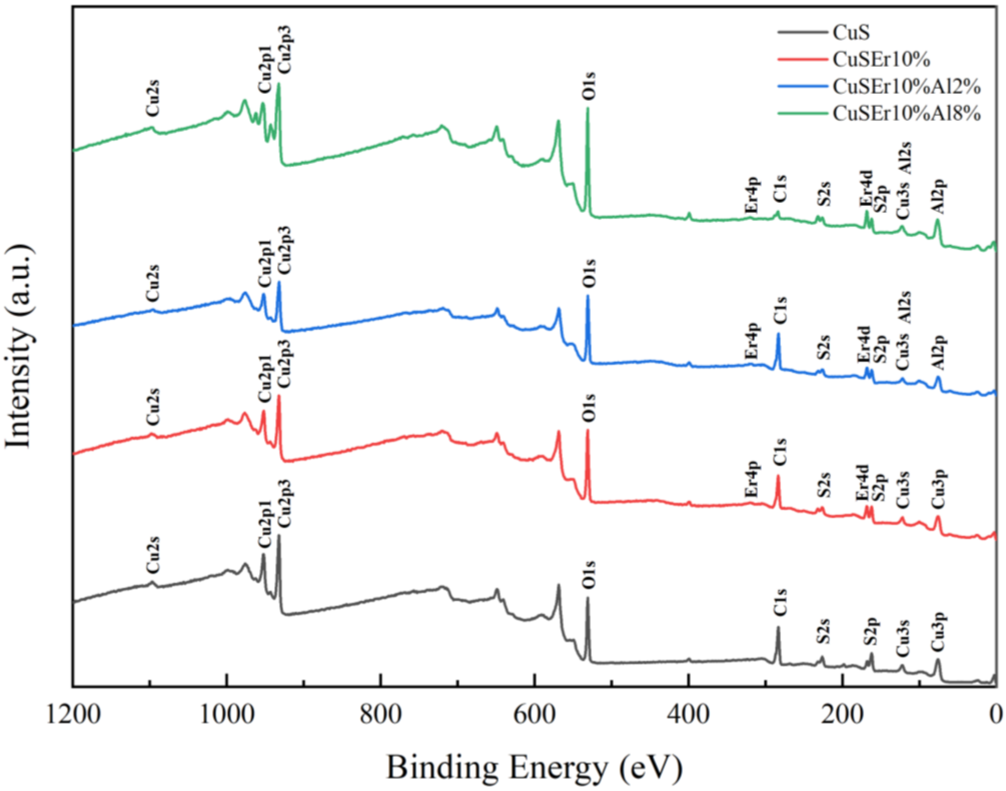

Fig. 3. XPS survey spectra of CuS and Er/Al co-doped CuS with different doping amounts of Al

Fig. 3 shows the XPS survey spectra of CuS and Er/Al co-doped CuS with different doping amounts of Al. This result confirmed the presence of Cu and S in CuS, the presence of Cu, S, and Er in Er-doped CuS, and the presence of Cu, S, Er, and Al in Er/Al co-doped CuS. Fig. 4a shows the peak signal of Er 4d at 163.78 eV, which can be referred to as the binding energy of Er^{3+} 4d 5/2 [43]. This result confirmed that Er^{3+} is the Er dopant ion. Moreover, there is a peak at 169.80 eV, which is indicated to be the binding energy of S^{2-} 2p 1/2, which confirms the bonding between Cu and S [44]. Fig. 4b shows the signal peaks at 76.6 eV and 77.6 eV for CuSEr10%Al2% and CuSEr10%Al8%, respectively, which refer to Al^{3+} 2p 3/2, confirming that Al^{3+} is in the lattice [45]-[47]. The slight shift in this binding energy further confirmed the difference in hole concentration, which can affect the bonding of Al ions in the lattice.

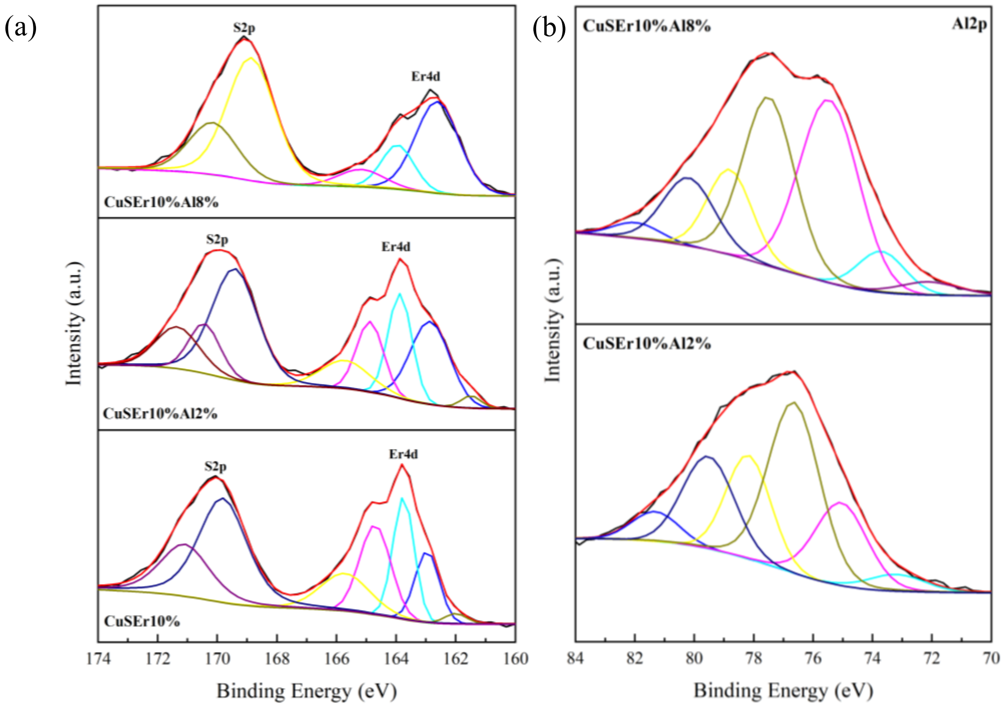

Fig. 4. XPS spectra of (a) S 2p core-level and Er 4d core-level of Er/Al co-doped CuS with different doping amounts of Al, and (b) Al 2p core-level of Er/Al co-doped CuS with different doping amounts of Al.

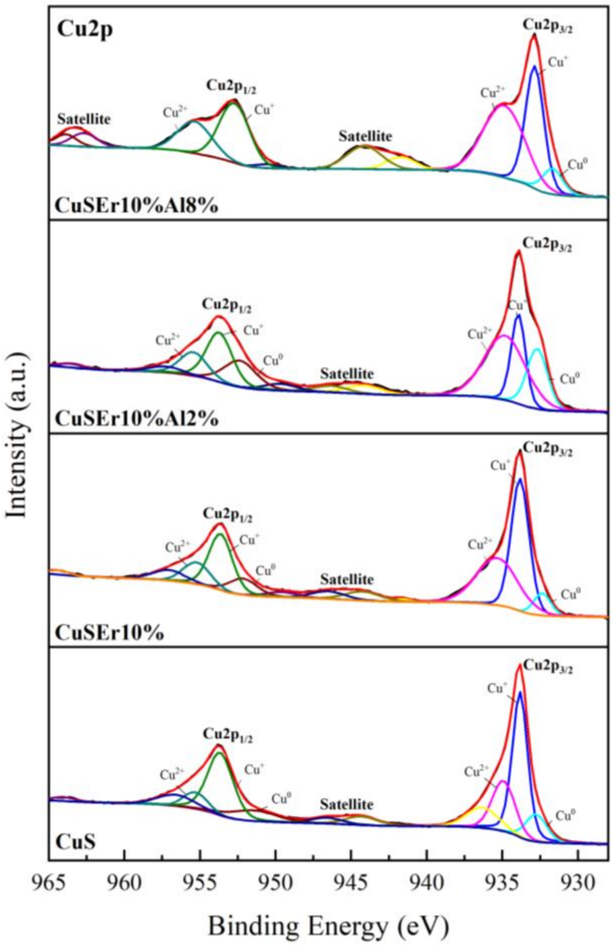

Fig. 5. XPS spectra of Cu 2p core-level of Er/Al co-doped CuS with different doping amounts of Al.

Fig. 5 shows XPS spectra of the Cu 2p core level of Er/Al co-doped CuS with different doping amounts of Al. There are six main peaks at approximately 955.38 eV, 953.72 eV, 951.12 eV, 934.98 eV, 933.82 eV, and 932.77 eV for the CuSEr10% and CuSEr10%Al2% samples, which are related to the CuS Cu 2p core-level peaks. The peaks at 952.12 eV and 932.77 eV were attributed to Cu^0. The peaks at 953.72 eV and 934.98 eV were attributed to Cu^+ 2p 1/2 and Cu^+ 2p 3/2, respectively, and the peaks at 955.38 eV and 933.82 eV were attributed to Cu^{2+} 2p 1/2 and Cu^{2+} 2p 3/2, respectively [48]. The ratio of Cu^+/Cu^{2+} was calculated to study the effect of hole concentration on the LSPR properties in the NIR region [38], as shown in Table 2.

Table 2. The Cu^+/Cu^{2+} contents ratio of CuS and Er/Al co-doped CuS with different doping amounts of Al.

Sample	CuS	CuSEr10%	CuSEr10%Al2%	CuSEr10%Al8%
Cu^+/Cu^{2+}	2.66	1.49	0.79	1.03

Table 2 shows the comparison of Cu^+/Cu^{2+} contents. Therefore, the Cu^+/Cu^{2+} content is decreasing before increasing at the CuSEr10%Al8% condition, which can be attributed to the oxidation and reduction of the hole carrier concentration in a different synthesis condition. The Cu^+/Cu^{2+} contents of CuSEr10%Al2% are the lowest value at 0.79. Assuming the Al^{3+} with a 0.53 Å ionic radius, which is approximately equivalent to Cu^{2+} with a 0.7 Å ionic radius, the substitution of Al^{3+} in Cu^{2+} is completely successful. The vacancy created an increasing hole carrier concentration. Leading to the oxidation of Cu^+ to Cu^{2+}, increasing the Cu^{2+} contents, and decreasing the Cu^+/Cu^{2+} ratio. Meanwhile, if the dopant is higher than appropriate, the Al^{3+} ions can enter the interstitial sites of the CuS lattice. Induced electrons in the crystal, causing the combination of Cu^{2+} and electrons, which led to the reduction of Cu^{2+} to Cu^+, further increased the Cu^+/Cu^{2+} ratio [38]. In summary, based on these structure and composition analyses of Er/Al co-doped CuS particles, Al^{3+} ions will preferentially substitute for Cu^{2+} sites within the CuS lattice due to their similar ionic radius, while Er^{3+} ions are more likely to occupy interstitial positions due to their relatively large ionic radius, which also leads to lattice distortion through interstitial incorporation. Alternative models for dopant position in Er/Al co-doped CuS are shown in Fig. 6.

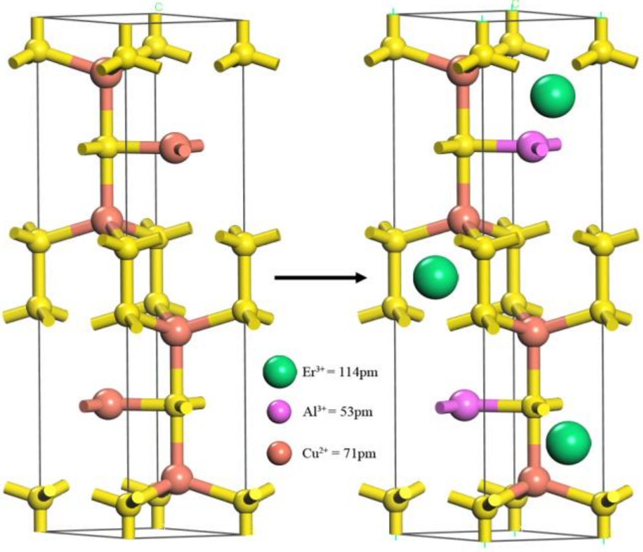

Fig. 6. Alternative models for dopants' position in Er/Al co-doped CuS.

3.2 Optical properties of CuS and Er/Al co-doped CuS particles

Fig. 7a illustrates the differences in absorbance between CuS and Er/Al co-doped CuS. Two absorption peaks at about 410nm and 705nm corresponded to the excitonic absorption of covellite CuS and interband transitions within the copper d-band, respectively [49], [50]. The red shift peak of interband transitions from ~705 nm to ~780 nm can be explained by changes in the local dielectric environment caused by the incorporation of Er^{3+} ions [51]. Meanwhile, the absorbance in the NIR range of Er/Al co-doped CuS is higher than that of CuS, indicating that the dopants influence the material's optical properties. To study further enhancement of optical properties of Er/Al co-doped CuS, a Tauc plot is plotted using the data from absorbance spectra to give an approximate band gap energy as calculated by formula 3.

$$(\alpha h\upsilon)^{\frac{1}{n}} = \beta(h\upsilon - E_g) \tag{3}$$

where α is the absorption coefficient, h is the Planck constant, v is the photon's frequency, E_g is the optical band gap energy, and A is a constant. The n factor depends on the nature of the electron transition and is equal to 1/2 or 2 for the direct allowed and indirect allowed transitions, respectively. The direct optical band gap of CuS is then obtained from the extrapolated linear region of a Tauc plot, as shown in Fig. 7b.

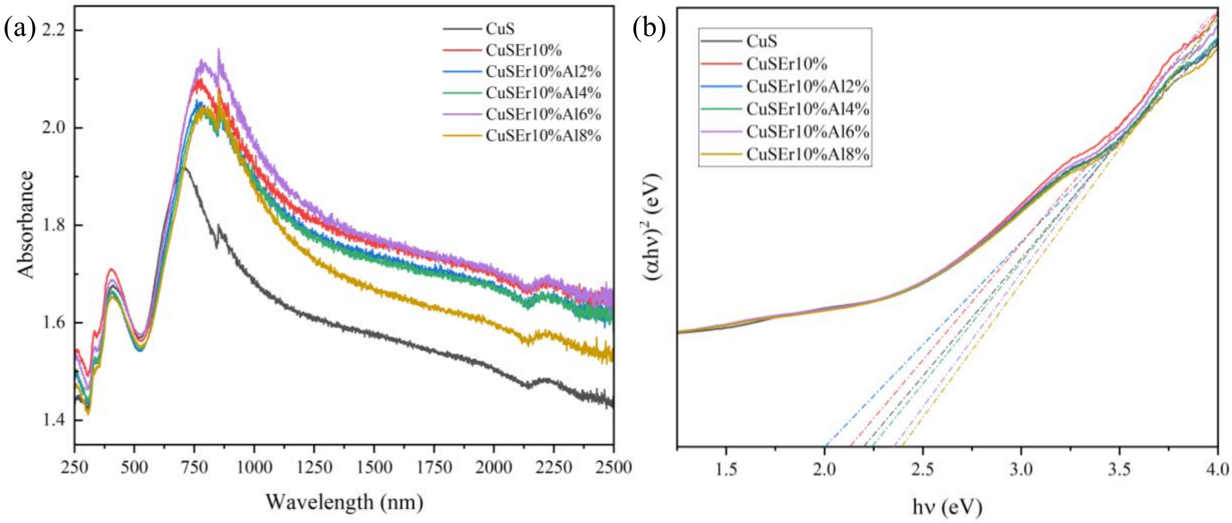

Fig. 7. Tauc plot calculation of all film samples with varied Sb dopant concentration and number of film coating layers

Table 3 shows the lower optical band gap energy trend when increasing the Al dopants to more than 2 mol%. The decrease in optical band gap energy can be used to ensure better performance of p-type semiconductors, which enhance LSPR properties in the NIR region of the material [52]. This can indicate that doping material with 2 mol% Al contents is causing Al ions to substitute with Cu ions, which have nearly the same ionic radius, creating holes, making it show the best performance of a p-type semiconductor. While higher dopant ratios of more than 2 mol% Al-doped can cause the interstitial of Al ions, creating free electrons in the lattice and lowering the p-type semiconductor properties of the material.

Table 3. Optical band gap energy of CuS and Er/Al co-doped CuS.

Sample	**CuS**	**CuSEr10%**	**CuSEr10% Al2%**	**CuSEr10% Al4%**	**CuSEr10% Al6%**	**CuSEr10% Al8%**
Band gap (eV)	2.20	2.13	2.00	2.24	2.35	2.40

3.3 Optical properties of CuS and Er/Al co-doped CuS films

Fig. 8 shows the transmittance spectra of all the samples compared with the uncoated glass slide and the coated glass slide with PVA. The trends of spectra are divided into three groups. This may be due to the difference in created hole concentration from the replacement of various dopant contents of dopants. To summarize the analysis, visible transmittance, NIR shielding value, and spectral performance are calculated using formulas 4 and 5, respectively [38]. The results are shown in Table 4.

$$T_{vis} = \frac{\sum_{400}^{800} T(\lambda)}{400} \tag{4}$$

$$S_{NIR} = 1 - \frac{\sum_{800}^{1500} T(\lambda)}{700} \tag{5}$$

where T_{vis} is visible transmittance of the film, S_{NIR} is NIR shielding value of the film and T(λ) is the optical transmittance obtained by UV–VIS–NIR spectrometer.

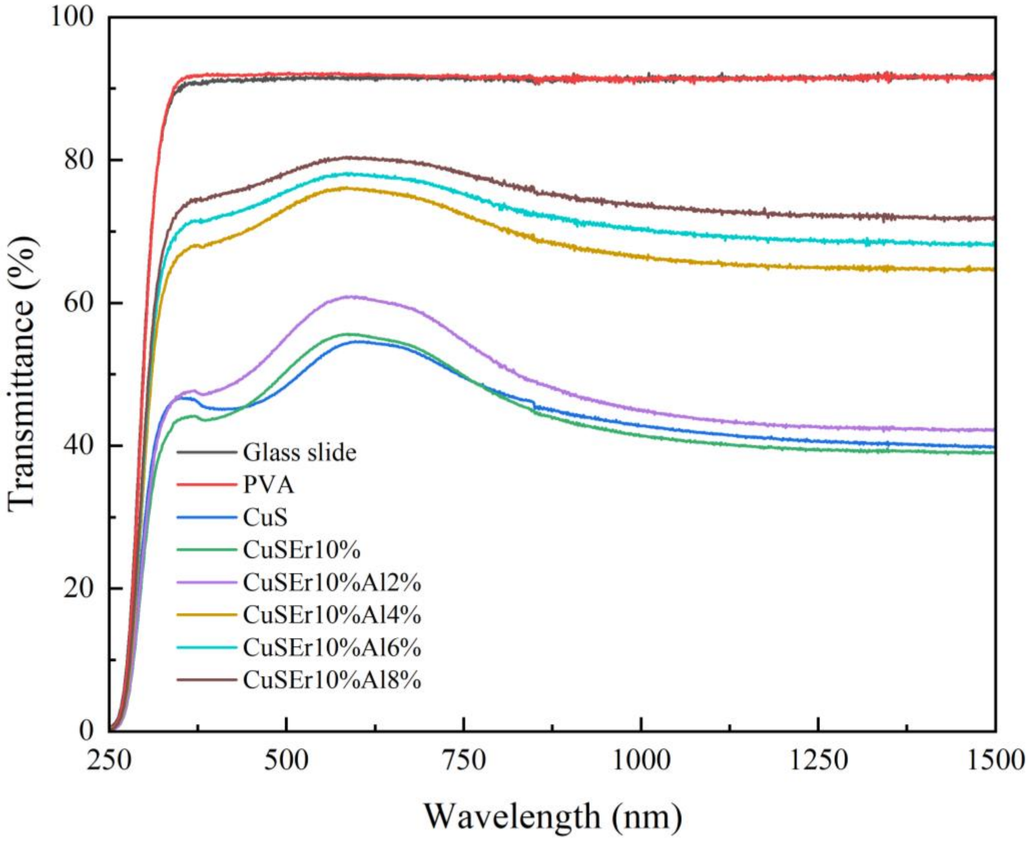

Fig. 8. UV–Vis–NIR transmittance spectra of CuS and Er/Al co-doped CuS with different doping amounts of Al.

Table 4 shows the increase of visible transmittance range from 50.5% to 78.7% and the decrease of NIR shielding value range from 26.8% to 59.1% according to the increase in Al doping. Considering the visible transmittance, NIR shielding value range, and spectral performance calculated from the difference of maximum transmittance in the visible region and minimum transmittance in the NIR region, CuSEr10%Al2% has the highest spectral performance with high visible transmittance at 56.2% and high NIR shielding value at 55.7%, which considered a high performance for NIR shielding application compared to Nimitnopphasit et al. (NIR shielding value at 50.1% for the highest spectral performance) [24]. This is consistent with the analysis results of p-type semiconductor material performance and LSPR in the NIR region performance obtained by comparing the optical band gap energy values of the materials in Table 3.

Table 4. Visible transmittance, NIR shielding value, and spectral performance of CuS and Er/Al co-doped CuS.

Sample	**Visible transmittance (%)**	**NIR shielding value (%)**	**Spectral performance**
CuS	50.5	58.0	Vis-max (54.6%) NIR-min (39.7%) Δ = 14.9 %
CuSEr10%	51.3	59.1	Vis-max (55.6%) NIR-min (38.8%) Δ = 16.8 %
CuSEr10%Al2%	56.2	55.7	Vis-max (61.0%) NIR-min (42.0%) Δ = 19.0 %
CuSEr10%Al4%	73.5	33.9	Vis-max (76.2%) NIR-min (64.3%) Δ = 11.9 %
CuSEr10%Al6%	76.0	30.2	Vis-max (78.2%) NIR-min (67.9%) Δ = 10.3 %
CuSEr10%Al8%	78.7	26.8	Vis-max (80.5%) NIR-min (71.3%) Δ = 9.2 %

3.4 Thermal shielding properties of CuS and Er/Al co-doped CuS films

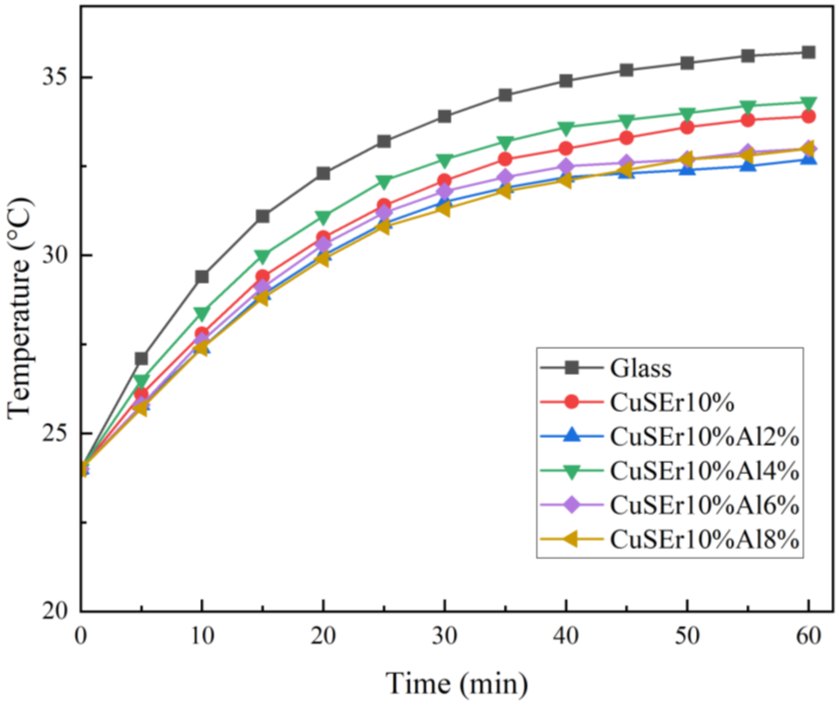

Fig. 9. The indoor temperatures of the heat box covered with different types of glasses.

Fig. 9 shows that under all film synthesis conditions, the temperature inside the heat box sharply increases while irradiated with an IR lamp at 1000 lux. The equilibrium temperature inside the heat box covered with uncoated glass, CuSEr10% film, CuSEr10%Al2% film, CuSEr10%Al4% film, CuSEr10%Al6% film, and CuSEr10%Al8% film is 35.7, 33.9, 32.7, 34.3, 33, and 33 °C, respectively.

The maximum difference in temperature inside the heat box between uncoated glass and coated glass is 3.0 °C for the CuSEr10%Al2% film. Due to the optimal Al doping, which can replace Cu ions and result in a vacancy of the hole carrier, the material exhibits the best LSPR properties in the near-infrared region [38]. The previous research has shown that the increase in the Earth's surface temperature by 1.0 °C results in an increase in annual electricity consumption by 9.2% [53]. The Er/Al co-doped CuS film of 10 mol% Er-doped CuS and 2 mol% Al-doped, which can reduce the heat inside the thermal simulation box by 3.0 °C, is a suitable material for further development to increase the efficiency of near-infrared radiation protection to reduce energy consumption in buildings.

4. Conclusion

Er/Al co-doped CuS particles were successfully synthesized by the co-precipitation method. XRD analysis confirms that all the samples had a hexagonal CuS structure with high crystallinity. The ratio of Cu^{+}/Cu^{2+} was calculated from the area ratio received from the XPS Cu 2p core-level analysis to confirm the change of Cu ion contents. The result shows that CuSEr10%Al2% has the lowest value at 0.79 due to its optimal hole carriers created, making this condition have the best LSPR property in the NIR region. Leading to the decreasing trend of optical band gap energy at the CuSEr10%Al2% condition, it also has the lowest optical band gap energy at 2.00 eV. The visible transmittance of Er/Al co-doped CuS films ranged from 51.3% to 78.7%. The NIR shielding value of Er/Al co-doped CuS films ranged from 59.1% to 26.8%. The highest spectral performance is 19.0% at the CuSEr10%Al2% condition, and the NIR shielding value of CuSEr10%Al2% is 55.7%, which is considered a high value. The glass coated with CuSEr10%Al2% films decreases the indoor temperature of the heat box by 3 °C. A one-degree Celsius increase in surface temperature leads to an increase in annual electricity consumption of 9.2%. Thus, Er/Al co-doped CuS can be considered a suitable material for development to improve the protection efficiency of nearby infrared radiation and further reduce indoor energy consumption.

Acknowledgments

This research was conducted at King Mongkut's Institute of Technology Ladkrabang. The authors would like to thank Nanocomposite Materials Research Laboratory (NMRL), School of Integrated Innovative Technology (SIITec), and King Mongkut's Institute of Technology Ladkrabang (KMITL) for the laboratory research.

References

[1] Ahmad, T., & Zhang, D. (2020). A critical review of comparative global historical energy consumption and future demand: The story told so far. *Energy Reports*, *6*, 1973–1991. DOI: 10.1016/j.egyr.2020.07.020.

[2] Alim, M. A., Tao, Z., Hassan, M. K., Rahman, A., Wang, B., Zhang, C., & Samali, B. (2019). Is it time to embrace building integrated Photovoltaics? A review with particular focus on Australia. *Solar Energy*, *188*, 1118–1133. DOI: 10.1016/j.solener.2019.07.002.

[3] Ke, Y., Zhou, C., Zhou, Y., Wang, S., Chan, S. H., & Long, Y. (2018). Emerging Thermal-Responsive Materials and Integrated Techniques targeting the Energy-Efficient Smart Window Application. *Advanced Functional Materials*, *28*(22), 1800113. DOI: 10.1002/adfm.201800113.

[4] Cai, L., Wu, X., Gao, Q., & Fan, Y. (2018). Effect of morphology on the near infrared shielding property and thermal performance of $K_{0.3}WO_3$ blue pigments for smart window applications. *Dyes and Pigments*, *156*, 33–38. DOI: 10.1016/j.dyepig.2018.03.074.

[5] Kumar, G. K., Saboor, S., & Babu, T. A. (2017). Study of various glass window and building wall materials in different climatic zones of India for energy efficient building construction. *Energy Procedia*, *138*, 580–585. DOI: 10.1016/j.egypro.2017.10.163.

[6] Ke, Y., Chen, J., Lin, G., Wang, S., Zhou, Y., Yin, J., Lee, P. S., & Long, Y. (2019). Smart Windows: electro-, thermo-, mechano-, photochromics, and beyond. *Advanced Energy Materials*, *9*(39), 1902066. DOI: 10.1002/aenm.201970153.

[7] Xu, X., Zhang, W., Hu, Y., Wang, Y., Lu, L., & Wang, S. (2017). Preparation and overall energy performance assessment of wide waveband two-component transparent NIR shielding coatings. *Solar Energy Materials and Solar Cells*, *168*, 119–129. DOI: 10.1016/j.solmat.2017.04.032.

[8] Sousa-Castillo, A., Ameneiro-Prieto, Ó., Comesaña-Hermo, M., Yu, R., Vila-Fungueiriño, J. M., Pérez-Lorenzo, M., Rivadulla, F., De Abajo, F. J. G., & Correa-Duarte, M. A. (2017). Hybrid plasmonic nanoresonators as efficient solar heat shields. *Nano Energy*, *37*, 118–125. DOI: 10.1016/j.nanoen.2017.05.014.

[9] Zhong, Q., Macharia, D. K., Zhong, W., Liu, Z., & Chen, Z. (2020). Synthesis of hydrophobic $W_{18}O_{49}$ nanorods for constructing UV/NIR-shielding and self-cleaning film. *Ceramics International*, *46*(8), 11898–11904. DOI: 10.1016/j.ceramint.2020.01.226.

[10] Li, B., Yao, J., Tian, S., Fang, Z., Wu, S., Liu, B., Gong, X., Tao, H., & Zhao, X. (2020). A facile one-step annealing route to prepare thermochromic W doped VO_2(M) particles for smart windows. *Ceramics International*, *46*(11), 18274–18280. DOI: 10.1016/j.ceramint.2020.05.042.

[11] Zhou, Q., Lv, W., Qiu, Q., Zhou, T., Huang, C., & Li, L. (2019). Boron doped M-phase VO_2 nanoparticles with low metal-insulator phase transition temperature for smart windows. *Ceramics International*, *46*(4), 4786–4794. DOI: 10.1016/j.ceramint.2019.10.211.

[12] Kim, K., Koo, B., & Ahn, H. (2019). Effects of Sb-doped SnO_2-WO_3 nanocomposite on electrochromic performance. *Ceramics International*, *45*(13), 15990–15995. DOI: 10.1016/j.ceramint.2019.05.109.

[13] Wang, S., Li, C., Tian, S., Liu, B., & Zhao, X. (2020). Facile synthesis of VO_2(D) and its transformation to VO_2(M) with enhanced thermochromic properties for smart windows. *Ceramics International*, *46*(10), 14739–14746. DOI: 10.1016/j.ceramint.2020.02.278.

[14] Yu, Z., Yao, Y., Yao, J., Zhang, L., Chen, Z., Gao, Y., & Luo, H. (2017). Transparent wood containing Cs_xWO_3 nanoparticles for heat-shielding window applications. *Journal of Materials Chemistry A*, *5*(13), 6019–6024. DOI: 10.1039/c7ta00261k.

[15] Takeda, H., Kuno, H., & Adachi, K. (2008). Solar control dispersions and coatings with Rare-Earth hexaboride nanoparticles. *Journal of the American Ceramic Society*, *91*(9), 2897–2902. DOI: 10.1111/j.1551-2916.2008.02512.x.

[16] Zhou, Y., Li, N., Xin, Y., Cao, X., Ji, S., & Jin, P. (2017). Cs_xWO_3 nanoparticle-based organic polymer transparent foils: low haze, high near infrared-shielding ability and excellent photochromic stability. *Journal of Materials Chemistry C*, *5*(25), 6251–6258. DOI: 10.1039/c7tc01616f.

[17] Lee, H. Y., Cai, Y., Bi, S., Liang, Y. N., Song, Y., & Hu, X. M. (2017). A Dual-Responsive Nanocomposite toward Climate-Adaptable Solar Modulation for Energy-Saving Smart Windows. *ACS Applied Materials & Interfaces*, *9*(7), 6054–6063. DOI: 10.1021/acsami.6b15065.

[18] Gao, Q., Wu, X., & Cai, L. (2019). Dual functionality of $K_{0.3}WO_3$/Ag_2O nanocomposites for smart window: Energy saving and visible photocatalytic self-cleaning performance. *Solar Energy Materials and Solar Cells*, *196*, 111–118. DOI: 10.1016/j.solmat.2019.03.042.

[19] Chen, Y., Zeng, X., Zhou, Y., Li, R., Yao, H., Cao, X., & Jin, P. (2017). Core-shell structured Cs_xWO_3@ZnO with excellent stability and high performance on near-infrared shielding. *Ceramics International*, *44*(3), 2738–2744. DOI: 10.1016/j.ceramint.2017.11.004.

[20] Wang, M., Bu, J., Xu, Y., Liu, Y., & Yang, Y. (2020). Sb-doped SnO_2 (ATO) hollow submicron spheres for solar heat insulation coating. *Ceramics International*, *47*(1), 547–555. DOI: 10.1016/j.ceramint.2020.08.162.

[21] Xiao, L., Su, Y., Qiu, W., Liu, Y., Ran, J., Wu, J., Lu, F., Shao, F., Tang, D., & Peng, P. (2016). Solar radiation shielding properties of transparent LaB6 filters through experimental and first-principles calculation methods. *Ceramics International*, *42*(12), 14278–14281. DOI: 10.1016/j.ceramint.2016.05.105.

[22] Shen, B., Wang, Y., Lu, L., & Yang, H. (2020). Synthesis and characterization of Sb-doped SnO_2 with high near-infrared shielding property for energy-efficient windows by a facile dual-titration co-precipitation method. *Ceramics International*, *46*(11), 18518–18525. DOI: 10.1016/j.ceramint.2020.04.157.

[23] Yao, Y., Zhang, L., Chen, Z., Cao, C., Gao, Y., & Luo, H. (2018). Synthesis of Cs_xWO_3 nanoparticles and their NIR shielding properties. *Ceramics International*, *44*(12), 13469–13475. DOI: 10.1016/j.ceramint.2018.04.158.

[24] Nimitnopphasit, P., Wattana, J., Kansaard, T., Mekprasart, W., Boonyarattanakalin, K., Jayasankar, C., & Phoohinkong, W. (2024). Physical and Optical Properties of Al/Yb-dually incorporated CuS Particles Prepared by Facile Co-precipitation Process. *Thai Journal of Nanoscience and Nanotechnology*, *9*(2), 11–21. DOI: 10.55003/tjnn9220242.

[25] Jiang, K., Chen, Z., & Meng, X. (2019). CuS and Cu_2S as Cathode Materials for Lithium Batteries: A Review. *ChemElectroChem*, *6*(11), 2825–2840. DOI: 10.1002/celc.201900066.

[26] Chen, X., Yang, J., Wu, T., Li, L., Luo, W., Jiang, W., & Wang, L. (2018). Nanostructured binary copper chalcogenides: synthesis strategies and common applications. *Nanoscale*, *10*(32), 15130–15163. DOI: 10.1039/c8nr05558k.

[27] Shamraiz, U., Hussain, R. A., & Badshah, A. (2016). Fabrication and applications of copper sulfide (CuS) nanostructures. *Journal of Solid State Chemistry*, *238*, 25–40. DOI: 10.1016/j.jssc.2016.02.046.

[28] Hsu, S., Bryks, W., & Tao, A. R. (2012). Effects of carrier density and shape on the localized surface plasmon resonances of $CU_{2-X}S$ nanodisks. *Chemistry of Materials*, *24*(19), 3765–3771. DOI: 10.1021/cm302363x.

[29] Wei, T., Liu, Y., Dong, W., Zhang, Y., Huang, C., Sun, Y., Chen, X., & Dai, N. (2013). Surface-Dependent localized surface plasmon resonances in CUS nanodisks. *ACS Applied Materials & Interfaces*, *5*(21), 10473–10477. DOI: 10.1021/am4039568.

[30] Rokade, A. A., Jin, Y. E., & Park, S. S. (2018). Facile synthesis of plate-like CuS nanoparticles and their optical and photo-thermal properties. *Materials Chemistry and Physics*, *207*, 465–469. DOI: 10.1016/j.matchemphys.2017.12.077.

[31] Kwon, Y., Lim, G., Kim, S., Ryu, S. H., Lim, H., & Choa, Y. (2017). Effect of localized surface plasmon resonance on dispersion stability of copper sulfide nanoparticles. *Applied Surface Science*, *477*, 204–210. DOI: 10.1016/j.apsusc.2017.11.006.

[32] Kwon, Y., Lim, G., Kim, S., Ryu, S. H., Hwang, T., Park, K., & Choa, Y. (2017). Near-infrared absorbance properties of $Cu_{2-x}S/SiO_2$ nanoparticles and their PDMS-based composites. *Journal of Materials Chemistry C*, *6*(4), 754–760. DOI: 10.1039/c7tc04784c.

[33] Kalanur, S. S., & Seo, H. (2018). Synthesis of Cu_xS Thin Films with Tunable Localized Surface Plasmon Resonances. *ChemistrySelect*, *3*(21), 5920–5926. DOI: 10.1002/slct.201800441.

[34] Luther, J. M., Jain, P. K., Ewers, T., & Alivisatos, A. P. (2011). Localized surface plasmon resonances arising from free carriers in doped quantum dots. *Nature Materials*, *10*(5), 361–366. DOI: 10.1038/nmat3004.

[35] Comin, A., & Manna, L. (2014). New materials for tunable plasmonic colloidal nanocrystals. *Chemical Society Reviews*, *43*(11), 3957–3975. DOI: 10.1039/c3cs60265f.

[36] Banumathi, T. V., & Sudha, J. S. (2021). Impact of doping transition metal in optically sensitive CuS with as prepared CuS. *AIP Conference Proceedings, 2369*(1), 020125. DOI: 10.1063/5.0061043.

[37] Gao, Q., Wu, X., & Huang, T. (2021). Novel energy efficient window coatings based on In doped CuS nanocrystals with enhanced NIR shielding performance. *Solar Energy*, *220*, 1–7. DOI: 10.1016/j.solener.2021.02.045.

[38] Gao, Q., Wu, X., & Huang, T. (2021). Greatly improved NIR shielding performance of CuS nanocrystals by gallium doping for energy efficient window. *Ceramics International*, *47*(17), 23827–23833. DOI: 10.1016/j.ceramint.2021.05.090.

[39] Bo, S., Hu, J., Wang, Q., Liu, X., & Zhen, Z. (2008). Near-infrared luminescence properties of erbium complexes with the substituted phthalocyaninato ligands. *Photochemical & Photobiological Sciences*, *7*(4), 474–479. DOI: 10.1039/b715809b.

[40] Hu, J. X., Karamshuk, S., Gorbaciova, J., Ye, H. Q., Lu, H., Zhang, Y. P., Zheng, Y. X., Liang, X., Hernández, I., Wyatt, P. B., & Gillin, W. P. (2018). High sensitization efficiency and energy transfer routes for population inversion at low pump intensity in Er organic complexes for IR amplification. *Scientific Reports*, *8*(1), 3226. DOI: 10.1038/s41598-018-21700-7.

[41] Jing, J., Gu, X., Zhang, S., Sun, J., Chen, Y., & Sun, T. (2019). Doping of aluminum (Al) into copper sulfide (CuS) nanocrystals enhanced their solar spectral selectivity. *CrystEngComm*, *21*(33), 4969–4975. DOI: 10.1039/c9ce00668k.

[42] Xie, Y., Chen, W., Bertoni, G., Kriegel, I., Xiong, M., Li, N., Prato, M., Riedinger, A., Sathya, A., & Manna, L. (2017). Tuning and Locking the Localized Surface Plasmon Resonances of CuS

(Covellite) Nanocrystals by an Amorphous CuPd$_x$S Shell. *Chemistry of Materials*, *29*(4), 1716-1723. DOI: 10.1021/acs.chemmater.6b05184.

[43] Guo, H., & Qiao, Y. M. (2008). Preparation, characterization, and strong upconversion of monodisperse $Y_2O_3:Er^{3+},Yb^{3+}$ microspheres. *Optical Materials*, *31*(4), 583–589. DOI: 10.1016/j.optmat.2008.06.011.

[44] Giribabu, K., Oh, S. Y., Suresh, R., Kumar, S. P., Manigandan, R., Munusamy, S., Gnanamoorthy, G., Kim, J. Y., Huh, Y. S., & Narayanan, V. (2016). Sensing of picric acid with a glassy carbon electrode modified with CuS nanoparticles deposited on nitrogen-doped reduced graphene oxide. *Microchimica Acta*, *183*(8), 2421–2430. DOI: 10.1007/s00604-016-1883-7.

[45] Li, X., Zhang, W., Sun, J., Liu, J., Hou, Y., Lin, L., He, K., & Yi, K. (2013). Influence of oxygen pressure and substrate temperature on the properties of aluminum fluoride thin films. *Applied Surface Science*, *282*, 226–230. DOI: 10.1016/j.apsusc.2013.05.108.

[46] Ram, S., & Mondal, A. (2003). X-ray photoelectron spectroscopic studies of Al^{3+} stabilized t-ZrO_2 of nanoparticles. *Applied Surface Science*, *221*(1–4), 237–247. DOI: 10.1016/s0169-4332(03)00883-3.

[47] Sanzaro, S., La Magna, A., Smecca, E., Mannino, G., Pellegrino, G., Fazio, E., Neri, F., & Alberti, A. (2016). Controlled AL^{3+} incorporation in the ZnO lattice at 188 °C by soft reactive Co-Sputtering for transparent conductive oxides. *Energies*, *9*(6), 433. DOI: 10.3390/en9060433.

[48] Jiang, J., Liu, X. X., Han, J., Hu, K., & Chen, J. S. (2021). Self-Supported Sheets-on-Wire $CuO@Ni(OH)_2/Zn(OH)_2$ Nanoarrays for High-Performance Flexible Quasi-Solid-State Supercapacitor. *Processes*, *9*(4), 680. DOI: 10.3390/pr9040680.

[49] Subramanyam, K., Sreelekha, N., Reddy, D. A., Murali, G., Ramanadha, M., Varma, K. R., Kumar, A. V., & Vijayalakshmi, R. P. (2017). Influence of Mn doping on structural, photoluminescence and magnetic characteristics of Covellite-Phase CuS nanoparticles. *Journal of Superconductivity and Novel Magnetism*, *31*(4), 1161–1165. DOI: 10.1007/s10948-017-4296-x.

[50] Ravele, M. P., Oyewo, O. A., & Onwudiwe, D. C. (2021). Controlled Synthesis of CuS and Cu_9S_5 and Their Application in the Photocatalytic Mineralization of Tetracycline. *Catalysts*, *11*(8), 899. DOI: 10.3390/catal11080899.

[51] Hosseinpour, Z., Alemi, A., Khandar, A. A., Zhao, X., & Xie, Y. (2015). A controlled solvothermal synthesis of CuS hierarchical structures and their natural-light-induced photocatalytic properties. *New Journal of Chemistry*, 39(7), 5470–5476. DOI: 10.1039/c4nj02298j.

[52] Faucheaux, J. A., Stanton, A. L. D., & Jain, P. K. (2014). Plasmon Resonances of Semiconductor nanocrystals: Physical principles and new Opportunities. *The Journal of Physical Chemistry Letters*, *5*(6), 976–985. DOI: 10.1021/jz500037k.

[53] Li, Y., Pizer, W. A., & Wu, L. (2018). Climate change and residential electricity consumption in the Yangtze River Delta, China. *Proceedings of the National Academy of Sciences*, *116*(2), 472–477. DOI: 10.1073/pnas.1804667115.